Nonlocal cancellation of dispersive broadening in Mach-Zehnder interferometers

Todd S. Larchuk
Department of Electrical Engineering, Columbia University, New York, New York 10027

Malvin C. Teich
Department of Electrical Engineering and Department of Applied Physics, Columbia University, New York, New York 10027

Bahaa E. A. Saleh
Department of Electrical, Computer and Systems Engineering, Boston University, Boston, Massachusetts 02215

We present theoretical and experimental second- and fourth-order interference patterns for entangled photons of different colors entering single and dual Mach-Zehnder interferometers in which dispersive elements have been deliberately placed. Although photon wave packets are generally broadened, as well as delayed, by passage through dispersive optical elements, coincidence measurements made with entangled photon pairs can be free of such broadening. This occurs for materials with particular dispersive behavior, as well as when the dispersion is balanced in both arms. This nonlocal behavior arises from the entanglement in the frequencies of the down-converted pair photons. We also show that nonlocal pump-frequency oscillations are present in the coincidence rate patterns for long path-length-difference times, confirming the robustness of this phenomenon in the presence of dispersion. However, the magnitude of these oscillations is reduced when an arbitrary dispersive material is used in an unbalanced configuration. Difference-frequency oscillations are also robust in the presence of dispersion, although they decay for large path-length-difference times.

PACS number(s): 42.50.−p

I. INTRODUCTION

It is well known that the entangled nature (nonfactorizable state) of the photon pair produced in parametric down-conversion results in a variety of nonlocal phenomena [1–3]. In an example recently discussed by Franson [4], the two photons of the pair can be detected in coincidence even when they are passed through separate dispersive elements.

A schematic diagram of the configuration envisioned by Franson [4] for displaying this effect is shown in Fig. 1. Photons from a laser pump beam are converted into entangled photon pairs by spontaneous parametric down-conversion in a $\chi^{(2)}$ nonlinear optical medium [1–5]. The photons of the entangled pair, created nearly simultaneously [6], exit the nonlinear medium in what are traditionally called signal and idler beams. They travel through two dispersive optical elements, with thicknesses z_1 and z_2, which impart phase shifts to them, before reaching two photon detectors (labeled DET A and DET B in Fig. 1). The individual photon wave packets are delayed and broadened in time by the dispersive elements in the same way that a classical electromagnetic pulse is broadened. Nevertheless, the photons remain coincident in the special case when their dispersion coefficients are equal in magnitude and opposite in sign [4]. This nonlocal behavior arises from the anticorrelation in the frequency components of the two photons, engendered by energy conservation.

Steinberg, Kwiat, and Chiao examined, from both a theoretical and an experimental point of view [7], the case in which only one of the photons of a degenerate entangled photon pair traversed a dispersive medium of thickness z_1, imparting a phase shift to the beam. This photon was then interfered with its twin at a single beam splitter before coincidence detection (see Fig. 2). Except for the dispersive element, this configuration is the same as that used by Hong, Ou, and Mandel [8] to demonstrate fourth-order interference at a beam splitter. The effect is revealed by the presence of a narrow dip in the coincidence rate, as one of the twin photons is delayed with respect to the other [8,9].

Shapiro and Sun [10] investigated the behavior of this configuration from a theoretical point of view, using quantum- and classical-field models for the signal and idler beams, in conjunction with the quantum and classical theories of photodetection, respectively. They showed that a small dispersion-free dip in the coincidence rate could be
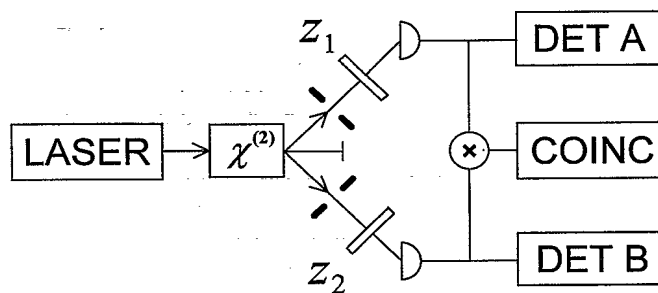

FIG. 1. Schematic diagram of the configuration envisioned by Franson [4]. Entangled photons, generated by spontaneous parametric down-conversion in a $\chi^{(2)}$ nonlinear optical medium, pass through dispersive optical elements of thicknesses z_1 and z_2, which introduce phase shifts. Photon detectors A and B record the events in the signal and idler beams, respectively, and coincidence events are monitored. For particular selections of the dispersive media, the photons remain coincident.
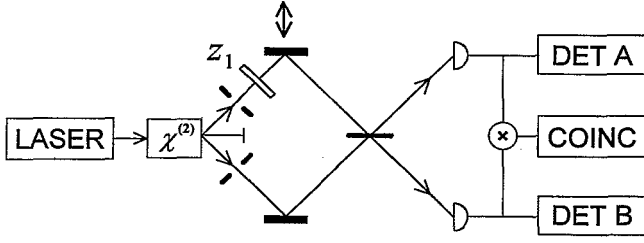
LARCHUK, TEICH, AND SALEH

FIG. 2. Schematic diagram of the configuration considered by Steinberg, Kwiat, and Chiao [7]. A dispersive element of thickness z_1, which introduces a frequency-dependent phase shift, is placed in one of the down-converted beams. This beam is also subjected to a variable path-length change relative to the other beam before they interfere in fourth order at a beam splitter. The narrow dip in the coincidence rate is not broadened by the presence of the dispersive element; its presence requires only that the centers of the wave packets meet simultaneously in the beam splitter.

FIG. 3. Schematic diagram of the MZI experiments considered in the present paper. Dispersive elements of thicknesses z_1 and z_2 are placed in one or both arms of the interferometer. The photons emerging from the ports of the interferometer are directed to photon detectors A and B. The detector output events are counted, both marginally and as coincidences, as the path-length-difference time τ is varied (by moving the mirror in the interferometer indicated with a double-edged arrow). Two MZI configurations were used. (a) The two beams overlapped fully within the interferometer; this condition is denoted full spatial overlap (FSO). (b) The two beams passed through the interferometer with no spatial overlap (NSO). The latter configuration was obtained by slightly rotating one of the mirrors that guides the light into the interferometer. It is equivalent to using two separate MZIs.

understood in terms of a classical pulse-compression effect arising from the integration time of the coincidence gate, but that the magnitude of the dip could be substantial only in the quantum theory. This dip then reflects the tendency of two indistinguishable photons to stick together [11] (it can become a null only for degenerate photons).

Since the occurrence of the dip depends only on the centers of the wave packets meeting simultaneously at the beam splitter [7], the subpicosecond measurement resolution of arrival-time differences of pair photons at a fourth-order beam-splitter interferometer is not degraded by the presence of the dispersive element. Dispersive elements more complex than a simple dielectric plate lead to similar results [12].

In this paper we examine the behavior of second- and fourth-order interference patterns, and in particular the non-local character of the coincidence rate, at the output of a dispersive Mach-Zehnder interferometer (MZI) into which down-converted beams are fed. We consider two MZI configurations. The first, shown in Fig. 3(a), has the two beams overlapping fully within the interferometer [denoted full spatial overlap (FSO)], whereas the second, shown in Fig. 3(b), has the two beams passing through the interferometer with no spatial overlap (NSO). This latter configuration is therefore equivalent to dual MZIs. Dispersive media with different thicknesses z_1 and z_2 introduce phase shifts into the optical beams traveling through the arms of the interferometer. The experimental arrangement is similar to that used in our earlier MZI measurements [13,14], except that in these experiments dispersion is purposely introduced.

The interference pattern is traced out by changing the path-length difference between the arms of the interferometer. This is effected by moving one of the interferometer mirrors (indicated by the double-sided arrows in Fig. 3). The output beams from the interferometer are directed to detectors A and B, as shown in the figure. The events at the detector outputs are counted during a time duration T, both marginally (in second order) and as coincidences (in fourth order), as a function of the path-length-difference time τ.

In Sec. II, the effects of dispersion on the second- and fourth-order interference patterns are considered from a theoretical point of view. Experimental results are provided in Sec. III. The conclusion is presented in Sec. IV.
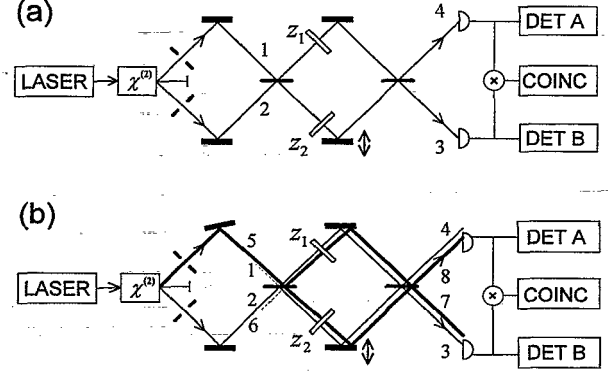
II. THEORY

The light at the inputs to the interferometer is represented by the state [11,15,16]

$$|\Psi_{ij}\rangle = \int_0^\infty \int_0^\infty \zeta(\omega,\omega')|1_{i\omega}\rangle|1_{j\omega'}\rangle d\omega \, d\omega' \quad , \qquad (1)$$

which approximately describes entangled photon pairs generated by parametric down-conversion excited into field modes (ports) i and j. The quantity $\zeta(\omega,\omega')$ is a joint complex amplitude characterizing a joint Gaussian spectral density function $|\zeta(\omega,\omega')|^2$ with center frequencies ω_1 and ω_2, marginal spectral widths σ, and correlation parameter $\eta = -1$ (representing complete anticorrelation as required by energy conservation). As illustrated in Fig. 3, $(i,j) \equiv (1,2)$ for the case of FSO, whereas $(i,j) \equiv (5,2)$ for NSO.

We calculate singles and coincidence rates using techniques similar to those employed by Campos, Saleh, and Teich [11]; they are modified by incorporating the (frequency-dependent) phase shifts imparted by the dispersive optical elements into the unitary transformation imposed on the input fields by the interferometer. The dispersive medium, along with the excess path length introduced by the movable mirror, imparts an excess phase shift to each beam. Defining $\beta(\omega)$ as the frequency-dependent propagation constant of light of angular frequency ω in the dispersive material, the excess phase shift is simply

$$\phi_{1,2}(\omega) = \omega\tau_{1,2} - \beta(\omega)z_{1,2} \quad , \qquad (2)$$

where $c_0\tau_{1,2}$ is the excess path length in vacuum with c_0 the speed of light in vacuum. It is assumed that only a single type of dispersive material is used in any experiment.

For most dispersive materials it is reasonable to assume that, within a narrow band of frequencies, ω around ω_1, and ω' around ω_2, $\beta(\omega)$ varies only slightly and gradually, in which case the analysis can be cast into familiar form by approximating $\beta(\omega)$ by the first three terms of a Taylor-series expansion about an appropriate center frequency, denoted ω_0 for convenience. In either of the beams, Eq. (2) then becomes [17]

$$\phi(\omega)|_{\omega\sim\omega_0}=\omega_0\tau-\beta_0(\omega_0)z+(\omega-\omega_0)[\tau-\beta_1(\omega_0)z]$$
$$-\tfrac{1}{2}(\omega-\omega_0)^2\beta_2(\omega_0)z \quad, \tag{3}$$

where

$$\beta_0(\omega_0)=\beta(\omega)|_{\omega=\omega_0}, \quad \beta_1(\omega_0)=d\beta(\omega)/d\omega|_{\omega=\omega_0},$$

$$\beta_2(\omega_0)=d^2\beta/d\omega^2|_{\omega=\omega_0} \quad. \tag{4}$$

A. Unbalanced dispersion

We first consider the case of unbalanced dispersion, in which a dispersive element of thickness z_2 is placed in the lower leg of the interferometer with no compensating dispersive element in the upper leg. Since the movable mirror is also in the lower leg, the excess phase shift in this leg is $\phi_2(\omega)=\omega\tau_2-\beta(\omega)z_2$ at frequency ω. The excess phase shift in the upper leg is $\phi_1(\omega)=0$. The net overall phase shift between the two paths of the interferometer is therefore $\phi(\omega)\equiv\phi_2(\omega)-\phi_1(\omega)=\omega\tau-\beta(\omega)z$, with $\tau\equiv\tau_2-\tau_1=\tau_2$ and $z\equiv z_2$.

For FSO [Fig. 3(a)] with 50%-50% beam splitters, in the nondegenerate case, we then calculate the probabilities of marginal photon detections, at ports 3 and 4, respectively, to be

$$P_3(\tau)=\tfrac{1}{2}+\tfrac{1}{4}[f(\tau,\omega_1)-f(\tau,\omega_2)] \quad, \tag{5}$$

$$P_4(\tau)=\tfrac{1}{2}-\tfrac{1}{4}[f(\tau,\omega_1)-f(\tau,\omega_2)] \quad, \tag{6}$$

where the quantity $f(\tau,\omega)$ depends on the center frequencies of the photon wave packets and is given by

$$f(\tau,\omega)=[1+\sigma^4\beta_2(\omega)^2z^2]^{-1/4}\exp\left\{\frac{-\sigma^2[\tau-\beta_1(\omega)z]^2}{2[1+\sigma^4\beta_2(\omega)^2z^2]}\right\}$$
$$\times\cos\left\{\omega\tau-\beta_0(\omega)z+\frac{\sigma^4\beta_2(\omega)z[\tau-\beta_1(\omega)z]^2}{2[1+\sigma^4\beta_2(\omega)^2z^2]}\right.$$
$$\left.-\frac{1}{2}\arctan[\sigma^2\beta_2(\omega)z]\right\} \quad. \tag{7}$$

The coincidence probability is

$$P_{34}(\tau)=\tfrac{1}{2}+\tfrac{1}{4}[g(\tau)+h(\tau)] \quad. \tag{8}$$

The quantity $g(\tau)$ consists of a contribution at the pump (or sum) frequency $(\omega_p=\omega_1+\omega_2)$ that does not decay with increasing path-length-difference time τ:

$$g(\tau)=\{1+\sigma^4[\beta_2(\omega_2)+\beta_2(\omega_1)]^2z^2\}^{-1/4}$$
$$\times\exp\left(\frac{-\sigma^2[\beta_1(\omega_2)-\beta_1(\omega_1)]^2z^2}{2\{1+\sigma^4[\beta_2(\omega_2)+\beta_2(\omega_1)]^2z^2\}}\right)$$
$$\times\cos\left(\omega_p\tau-[\beta_0(\omega_2)+\beta_0(\omega_1)]z\right.$$
$$+\frac{\sigma^4[\beta_2(\omega_2)+\beta_2(\omega_1)]z[\beta_1(\omega_2)-\beta_1(\omega_1)]^2z^2}{2\{1+\sigma^4[\beta_2(\omega_2)+\beta_2(\omega_1)]^2z^2\}}$$
$$\left.-\frac{1}{2}\arctan\{\sigma^2[\beta_2(\omega_2)+\beta_2(\omega_1)]z\}\right) \quad, \tag{9}$$

whereas the quantity $h(\tau)$ consists of a contribution at the difference frequency $\omega_d=\omega_2-\omega_1$ that does decay with increasing τ:

$$h(\tau)=\{1+\sigma^4[\beta_2(\omega_2)-\beta_2(\omega_1)]^2z^2\}^{-1/4}\exp\left(\frac{-2\sigma^2\{\tau-\tfrac{1}{2}[\beta_1(\omega_2)+\beta_1(\omega_1)]z\}^2}{\{1+\sigma^4[\beta_2(\omega_2)-\beta_2(\omega_1)]^2z^2\}}\right)\cos\left(\omega_d\tau-[\beta_0(\omega_2)-\beta_0(\omega_1)]z\right.$$
$$+\frac{2\sigma^4[\beta_2(\omega_2)-\beta_2(\omega_1)]z\{\tau-\tfrac{1}{2}[\beta_1(\omega_2)+\beta_1(\omega_1)]z\}^2}{\{1+\sigma^4[\beta_2(\omega_2)-\beta_2(\omega_1)]^2z^2\}}-\frac{1}{2}\arctan\{\sigma^2[\beta_2(\omega_2)-\beta_2(\omega_1)]z\}\right) \quad. \tag{10}$$

For NSO [Fig. 3(b)] with 50%-50% beam splitters, these probabilities are, at ports 3 and 8, respectively,

$$P_3(\tau)=\tfrac{1}{2}-\tfrac{1}{2}f(\tau,\omega_2) \quad, \tag{11}$$

$$P_8(\tau)=\tfrac{1}{2}-\tfrac{1}{2}f(\tau,\omega_1) \quad, \tag{12}$$

and

$$P_{38}(\tau)=\tfrac{1}{4}-\tfrac{1}{4}[f(\tau,\omega_1)+f(\tau,\omega_2)]+\tfrac{1}{8}[g(\tau)+h(\tau)], \tag{13}$$

where $f(\tau)$, $g(\tau)$, and $h(\tau)$ are as defined in Eqs. (7), (9), and (10) above.

The quantities $f(\tau)$, $g(\tau)$, and $h(\tau)$ all take the form of a product of three factors: the first is a constant, the second is a Gaussian function of τ [except for $g(\tau)$, where this factor is also constant], and the third is a harmonic function of τ whose phase is a second-order polynomial in τ [again, except

for $g(\tau)$]. The first factor, which depends on $\sigma^2\beta_2 z$, simply serves to reduce the magnitude of all three components. For $f(\tau)$, which determines the singles rates and contributes to the coincidence rate for NSO, the Gaussian function is translated in path-length-difference time τ by the value $\beta_1 z$. For $h(\tau)$, which is the difference-frequency contribution to the coincidence rates, the Gaussian function is similarly translated by $\beta_1 z$, but with a value of β_1 that is the mean of those at the two center frequencies. Both of these Gaussian functions are broadened by a factor that depends on $\sigma^2\beta_2 z$. For $g(\tau)$, which is the pump-frequency contribution to the coincidence rates, the Gaussian is independent of τ and its presence therefore simply serves to modify the magnitude of the contribution. The harmonic functions associated with $f(\tau)$, $g(\tau)$, and $h(\tau)$ vary with respect to the path-length-difference time τ, respectively, at the individual wave-packet center frequencies, the pump frequency, and the difference frequency. All exhibit a phase shift that depends on $\beta_0 z$ and $\sigma^2\beta_2 z$, and a chirp that depends on $\sigma^2\beta_2 z$. Setting $z = 0$ in Eqs. (7), (9), and (10) leads to results for Eqs. (5), (6), (8), and (11)–(13) that accord with those obtained previously in the absence of dispersion [11,13].

B. Balanced dispersion

We now consider the case of balanced dispersion, in which dispersive elements of identical thicknesses $z = z_2 = z_1$ are placed in both legs of the interferometer. The excess phase shift in the lower leg is then $\phi_2(\omega) = \omega\tau_2 - \beta(\omega)z_2$, whereas the excess phase shift in the upper leg is $\phi_1(\omega) = -\beta(\omega)z_1$. The net overall phase shift between the two paths of the interferometer is then $\phi_{\text{bal}}(\omega) \equiv \phi_2(\omega) - \phi_1(\omega) = \omega\tau$, where again $\tau = \tau_2$. This is true whether the system is quantum mechanical or classical.

The results are therefore identical to those obtained in the nondispersive case, i.e., a complete cancellation of dispersion occurs both in second and in fourth order. Thus the second-order interference patterns for balanced dispersion reveal oscillations at one, or both, of the center frequencies of the photons (depending on whether the interferometer is operated with NSO or FSO) and these die away when the path-length-difference time exceeds the second-order coherence time.

For short path-length-difference times, the fourth-order interference patterns (coincidence rates) exhibit spectral components at the difference and sum of the center frequencies of the photon wave packets for both FSO and NSO; in the case of NSO, individual spectral components at ω_1 and ω_2 are also present. Finally, for both FSO and NSO, the coincidence rate exhibits pump-frequency oscillations that extend to path-length-difference times that exceed the second-order coherence times and indeed continue indefinitely in the ideal case.

C. Examples

The significance of the theoretical results is perhaps best illustrated by graphical example. In Fig. 4 we present a quartet of plots of the marginal and coincidence detection probabilities for full spatial overlap [schematized in Fig. 3(a)]. The four quadrants of the plot represent different values of the dispersion medium thickness z_2. In all cases $z_1 = 0$ so

that the dispersion is unbalanced. Graphs are presented for the marginal detection probability $P_3(\tau)$ at detector B [Eqs. (5) and (7)] and for the coincidence detection probability $P_{34}(\tau)$[Eqs. (8)–(10)] vs the path-length-difference time τ of the interferometer. Graphs for the marginal detection probability $P_4(\tau)$ at detector A [Eq. (6)] are not shown since they differ from those of $P_3(\tau)$ only by a phase factor. The details of the harmonic variation, such as chirping, are not observable at this scale.

These plots were generated using numerical values that are appropriate for the experiments reported in Sec. III. The pump-beam wavelength was fixed at $\lambda_p = 413.1$ nm and the signal-beam wavelength at $\lambda_1 = 840.0$ nm; energy conservation then set the idler-beam wavelength at $\lambda_2 = 812.8$ nm. The radian-frequency bandwidths of both the signal and idler beams were chosen to be $\sigma = 1.25 \times 10^{13}$ s^{-1}. The dispersive material was taken to be Schott type-BK7 glass. A fourth-order polynomial fit to the refractive-index values tabulated for this glass in the Schott Optical Glass Catalog [18] was used to estimate the values of the group velocities and dispersion coefficients, which, of course, depend on the frequency about which the expansion is made. For $\lambda = 840.0$ nm, we obtained $\beta_0 = 1.1300 \times 10^7$ m^{-1}, $\beta_1 = 5.0914 \times 10^{-9}$ s m^{-1}, and $\beta_2 = 1.5580 \times 10^{-26}$ s^2 m^{-1}; for $\lambda = 812.8$ nm we obtained $\beta_0 = 1.1681 \times 10^7$ m^{-1}, $\beta_1 = 5.0927 \times 10^{-9}$ s m^{-1}, and $\beta_2 = 1.8077 \times 10^{-26}$ s^2 m^{-1}.

The result calculated for the nondispersive case $(z_1 = z_2 = 0)$ is shown in the upper-left quadrant of Fig. 4. Both the marginal response registered by detector B and the coincidence response are centered symmetrically about the balanced path-length-difference time $\tau = 0$. These results are identical to those calculated [11] and measured [13] previously (with use of the appropriate parameters). They are also applicable for the balanced dispersion case as discussed above.

The result computed for a 2.54-cm-thick glass plate inserted in the lower arm of the interferometer is shown in the upper-right quadrant of Fig. 4. As a result of first-order dispersion, the center frequencies of the marginal and coincidence oscillations are translated to a higher path-length-difference time by the amount $\beta_1 z$, so that the center lies at $\tau = 129.34$ ps. As in the absence of dispersion, the oscillations registered by detector B comprise a superposition of the two individual photon wave packets. Aside from the shift, the patterns are virtually indistinguishable from those without dispersion for this thickness of glass. Thus the presence in the apparatus of a few centimeters of a dispersive material, such as a corner-cube beam splitter, is expected to have little effect on the behavior of the system. In particular, the sum-frequency oscillations persist.

The results for $z_2 = 25.4$ cm, an increase of a factor of 10, are shown in the lower-left quadrant. As expected, the center is shifted to 1293.4 ps. The significant separation of the wave packets alters the shape of the interference pattern substantially. The coincidence rate continues to reveal difference-frequency oscillations that decay. The pump-frequency oscillations do not decay, but their visibility is reduced relative to that of the nondispersive case. Only for the special case $\beta_1(\omega_1) = \beta_1(\omega_2)$ and $\beta_2(\omega_1) = -\beta_2(\omega_2)$ do the pump-frequency oscillations have the same visibility as in the absence of dispersion, as is evident from Eq. (9).
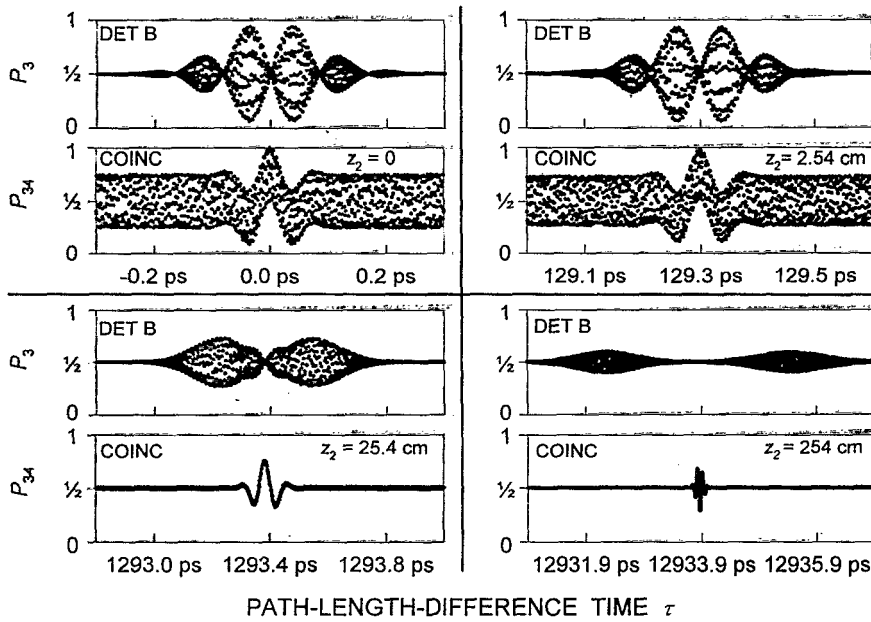
PATH-LENGTH-DIFFERENCE TIME τ

FIG. 4. Marginal and coincidence detection probabilities for full spatial overlap [schematized in Fig. 3(a)]. Graphs are presented for the marginal detection probability $P_3(\tau)$ at detector B and for the coincidence detection probability $P_{34}(\tau)$, vs the path-length-difference time τ of the interferometer. The four quadrants of the plot represent different values of dispersion-medium (BK7 glass) thickness z_2. In all cases $z_1 = 0$ so that the dispersion is unbalanced. The figures do not have sufficient resolution to make the details of the harmonic variation, such as chirping, discernible at the scale shown.

Finally, the interference pattern computed for 254 cm of glass is displayed in the lower-right quadrant of Fig. 4. As expected, the center is shifted yet higher to 12 934 ps. The thickness of the glass in the lower-right quadrant is sufficiently large so that the individual wave packets are completely separated. The pump-frequency oscillations remain, but their visibility diminishes further as more (unbalanced) dispersion is introduced, in accordance with the calculated result.

Almost imperceptible in these graphs is the broadening of the envelopes of the individual wave packets, and of the difference-frequency oscillations, arising from second-order dispersion $(\sigma^2 \beta_2 z)$, as evidenced by the denominators of the Gaussian exponents in Eqs. (7) and (10), respectively. This broadening is not present in the coincidence rate when $\beta_2(\omega_1) = \beta_2(\omega_2)$.

In Fig. 5 we present the analogous plots for no spatial overlap [schematized in Fig. 3(b)]. Graphs are presented for the marginal detection probabilities $P_3(\tau)$ at detector B and $P_8(\tau)$ at detector A [Eqs. (11), (12), and (7)], as well as the coincidence detection probability $P_{38}(\tau)$ [Eqs. (13), (7), (9), and (10)], vs the path-length-difference time τ. The parameter values are identical to those used in Fig. 4.

The results for the nondispersive case $(z_1 = z_2 = 0)$, in the upper-left quadrant of Fig. 5, are again identical to those reported previously (with appropriate choice of parameters) [11,13]. They are also applicable for the balanced dispersion case as discussed above. Each of the detectors "sees" a different photon wave packet. The coincidence response contains oscillations at the pump, difference, and individual frequencies.

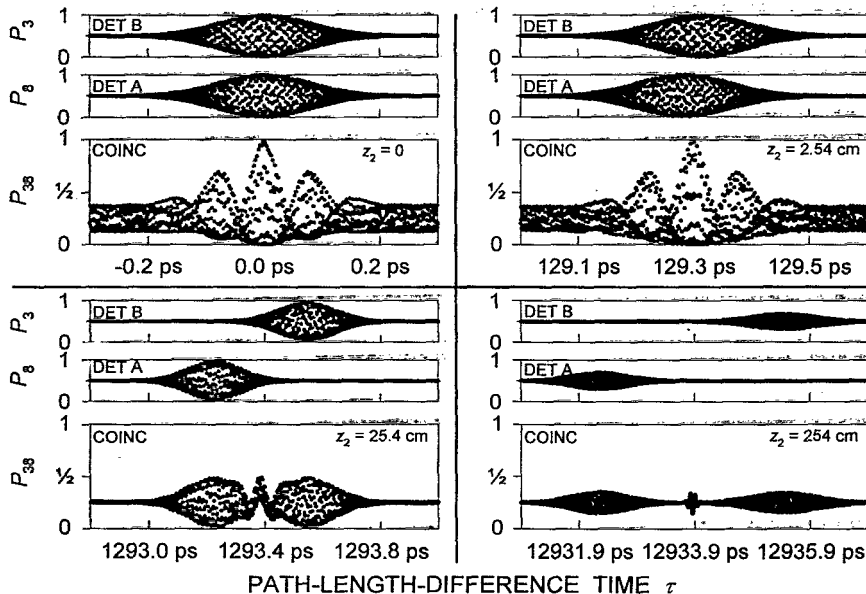PATH-LENGTH-DIFFERENCE TIME τ

FIG. 5. Marginal and coincidence detection probabilities for no spatial overlap [schematized in Fig. 3(b)]. Graphs are presented for the marginal detection probabilities $P_3(\tau)$ at detector B and $P_8(\tau)$ at detector A, along with the coincidence detection probability $P_{38}(\tau)$, vs the path-length-difference time τ. The four quadrants represent different values of dispersion-medium (BK7 glass) thickness z_2. In all cases $z_1 = 0$ so that the dispersion is unbalanced. The figures do not have sufficient resolution to make the details of the harmonic variation, such as chirping, discernible at the scale shown.
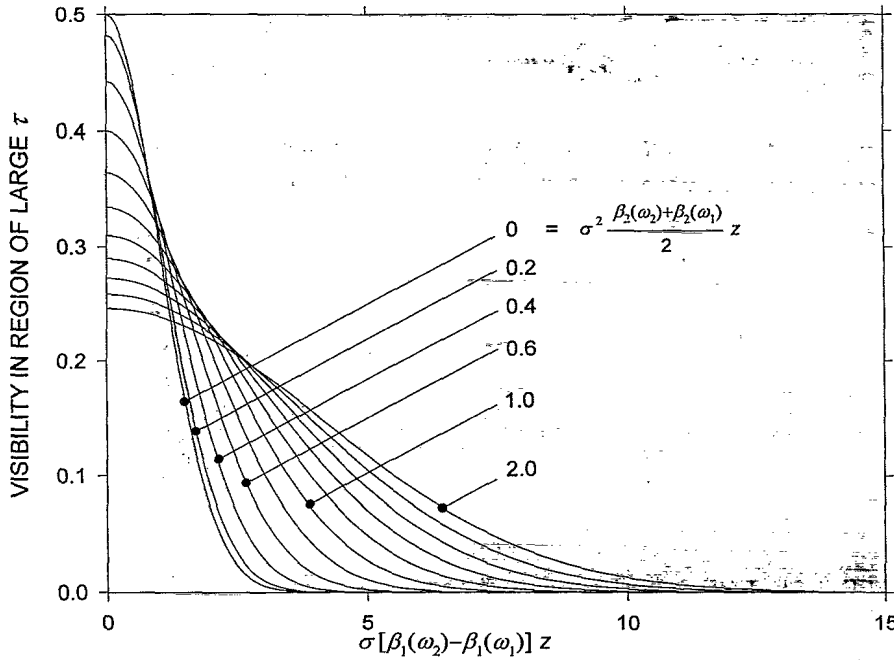
FIG. 6. Visibility of the pump-frequency oscillations in the limit of large τ, for both full spatial overlap and no spatial overlap, as a function of the parameters in Eq. (9): $\sigma[\beta_1(\omega_2) - \beta_1(\omega_1)]z$ and $\frac{1}{2}\sigma^2[\beta_2(\omega_2) + \beta_2(\omega_1)]z$.

The computed result for a 2.54-cm-thick glass plate inserted in the lower arm of the NSO interferometer is shown in the upper-right quadrant of Fig. 5. As a result of first-order dispersion, the two marginal responses appear at slightly different path-length-difference times, but the patterns are virtually indistinguishable from those without dispersion. Again, the sum-frequency oscillations persist.

The interference patterns computed for 25.4 and 254 cm of glass are displayed in the lower-left and lower-right quadrants of Fig. 5. Their centers are shifted to 1293.4 and 12934 ps, respectively, and the difference-frequency oscillations in the coincidence rate remain centered at the mean value, just as in the case of FSO. The thickness of the glass in the lower-right quadrant is sufficiently large such that the two individual wave packets are completely separated. The decrease in magnitude imparted by second-order dispersion, through the first factor in Eq. (7), is noticeable at the largest thickness.

The coincidence rate reveals the presence of the individual wave packets, difference-frequency oscillations that decay as τ increases, and pump-frequency oscillations that do not decay. As with FSO, only for the special case $\beta_1(\omega_1) = \beta_1(\omega_2)$ and $\beta_2(\omega_1) = -\beta_2(\omega_2)$ do the pump-frequency oscillations have the same visibility as in the absence of dispersion. There is some broadening of the envelopes of the individual wave packets and of the difference-frequency oscillations, arising from second-order dispersion (through the quantity $\sigma^2\beta_2 z$), just as in the case of FSO.

The hallmark of nonlocal fourth-order interference in the MZI is the presence of pump-frequency oscillations for arbitrarily large path-length-difference times [11,13,14]. It is therefore of special interest to examine the effect of dispersion on these oscillations.

The coincidence rates for FSO and NSO are given by Eqs. (8) and (13), respectively. For sufficiently large values of τ, the quantities $f(\tau)$ and $h(\tau)$ in Eqs. (7) and (10) disappear. In this limit, we obtain $P_{34}(\tau) = \frac{1}{2} + \frac{1}{4}g(\tau)$ for FSO and

$P_{38}(\tau) = \frac{1}{4} + \frac{1}{8}g(\tau)$ for NSO so that the essential behavior of the nonlocal pump-frequency oscillations in the presence of dispersion are contained in the quantity $g(\tau)$ provided in Eq. (9). Since the first and second factors in this equation depend on the parameters $\sigma[\beta_1(\omega_2) - \beta_1(\omega_1)]z$ and $\frac{1}{2}\sigma^2[\beta_2(\omega_2) + \beta_2(\omega_1)]z$, Fig. 6 presents the parametric dependence of the visibility on these quantities. The curves in Fig. 6 apply for both FSO and NSO and the maximum value of the visibility is $\frac{1}{2}$ in both cases. As the dispersion coefficients β_2 become larger, an increased difference in the group velocities β_1 can be tolerated to achieve a given value of visibility.

III. EXPERIMENT

We have conducted a set of experiments to examine the second- and fourth-order interference patterns using entangled photon pairs produced by parametric down-conversion in the dispersive MZI.

A. Experimental arrangement

The experimental arrangement is shown in Fig. 3. A Coherent Model 302 krypton-ion laser, operated on the 413.1-nm violet line, served as the pump. An intracavity étalon ensured that the laser operated on a single longitudinal mode and the spatial aperture was adjusted to obtain $TEM_{0,0}$ transverse-mode operation. The optical power at the laser output was set at 100 mW and power stabilization and mode stabilization were activated.

After attenuation by a neutral-density filter, approximately 1 mW of pump power was focused onto a 10-mm-long lithium iodate ($LiIO_3$) down-conversion crystal oriented for type-I (ooe) phase matching, with the extraordinary-polarized pump incident at 42.8° to the optic axis of the crystal. Unconverted pump photons passed straight through the crystal and into a beam dump.
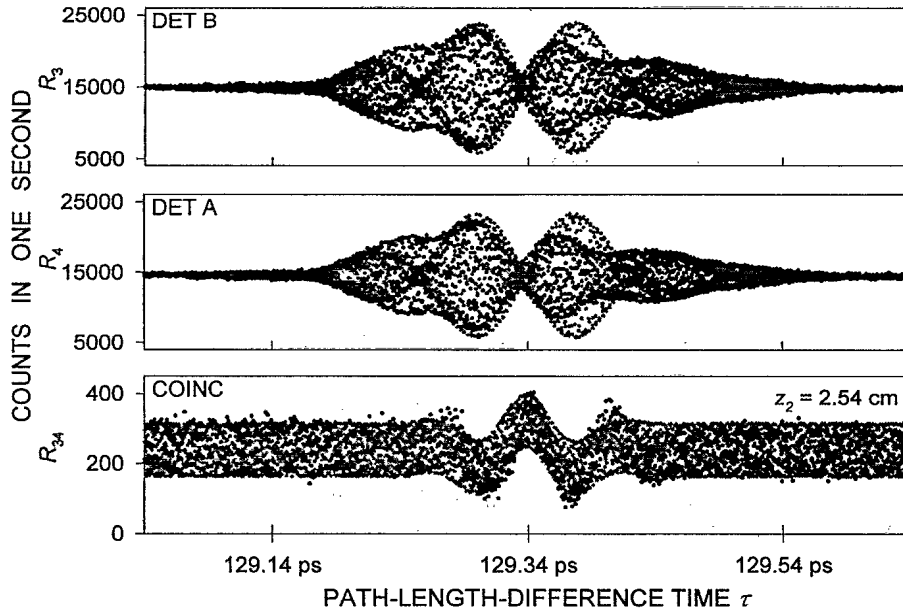
FIG. 7. Mach-Zehnder interference patterns for unbalanced dispersion with FSO. Experimental data (black dots) and theoretical results (gray dots) with $z_2 = 2.54$ cm of BK7 glass inserted in one arm of the interferometer ($z_1 = 0$). The upper panel shows the counts recorded by detector B, the middle panel shows the counts recorded by detector A, and the lower panel shows the counts recorded in coincidence between detectors A and B. The vertical scale represents the number of counts recorded in 1 s for each path-length-difference time τ (corresponding to a different position of the retroreflector).

Down-converted photons emerge at an angle to the pump beam, with degenerate photons emerging symmetrically in a cone with a (external) half angle of about 9°; in most of our experiments, however, we used nondegenerate photons, which emerge asymmetrically in accordance with the energy- and phase-matching conditions. With apertures of about 2 mm diameter, we selected out desired nondegenerate photon pairs with center frequencies of about 813 and 840 nm. The statistics of the marginal and coincidence detections using this arrangement have been discussed previously [19].

The photons were then directed, by mirrors, into the two input ports of the interferometer. The actual experiment made use of a folded Mach-Zehnder interferometer in which the beams were redirected onto a lower portion of the same beam-splitter cube by two retroreflectors. One of the retroreflectors was mounted on a movable translation stage used to change the path-length-difference time for the two interferometer arms. For the unbalanced-dispersion experiments, a $\frac{1}{2}$-in.-thick plate of BK7 glass was inserted into the movable arm of the interferometer (thus $z_2 = 2.54$ cm since the beam makes a double pass through the glass). In the balanced-dispersion experiment, a $\frac{1}{2}$-in.-thick plate of BK7 glass was inserted into each arm of the interferometer ($z_1 = z_2 = 2.54$ cm).

By adjusting the angle of one of the input mirrors, the photon's paths within the interferometer could be made to exhibit either FSO [Fig. 3(a)] or NSO [Fig. 3(b)]. For both types of experiment, the path length of only one arm of the interferometer was varied (by changing the position of the movable retroreflector).

The photons exiting the interferometer were passed through focusing lenses and a pair of RG-695 filters to block the pump light and then allowed to impinge onto two custom-configured single-photon counting modules (RCA type SPCM-100; now sold by EG&G). At the heart of these detectors lie passively quenched avalanche photodiodes whose diameter for peak photon-detection efficiency is about 100 μm.

After suitable compensation for electronic delay differences, the signals from the two photon-counting modules were sent to a pair of Berkeley Nucleonics Corp. type 8010 pulse generators that produced standardized 10-ns-wide pulses triggered by the leading edges of the detector-module outputs. These standardized pulses were then sent to the dual inputs of a Stanford Research Systems type SR400 Two-Channel Gated Photon Counter and counted for 1 s to provide a measure of the rate of photon detections at each of the output ports. They were also added together and sent to a Hewlett-Packard type 5370A Universal Time-Interval Counter, which, triggered by the gated photon counter, counted for 1 s to provide a measure of the coincidence rate.

B. Unbalanced dispersion

The interference patterns for unbalanced dispersion, with $z_2 = 2.54$ cm and $z_1 = 0$, are presented in Figs. 7 and 8 for FSO and NSO, respectively. The upper panels show the counts recorded by detector B (at output port 3), the middle panels show the counts recorded by detector A (at output port 4 for FSO and output port 8 for NSO), and the lower panels show the coincidence counts (at output ports 3 and 4 for FSO and at output ports 3 and 8 for NSO). The black data points fill out the envelopes of the interference patterns but do not have the resolution to trace out the harmonic variation at the scale of the figure. All of the data in each figure were collected in the same experimental run.

The data in Figs. 7 and 8 may be compared with the theoretical results embodied in Eqs. (5), (6), (8), and (11)–(13). The upper-right quadrants of Figs. 4 and 5 are the probabilities for marginal and coincidence detections obtained by applying these formulas using the experimental parameters. The comparison is facilitated by renormalizing the theoretical formulas to account for imperfect visibilities and the fact that the data were collected as a sequence of a large number of measurements:

$$R_3(\tau) = N_3 \left\{ \frac{1}{2} + \frac{V_3}{4} [f(\tau, \omega_1) - f(\tau, \omega_2)] \right\} , \quad (5')$$
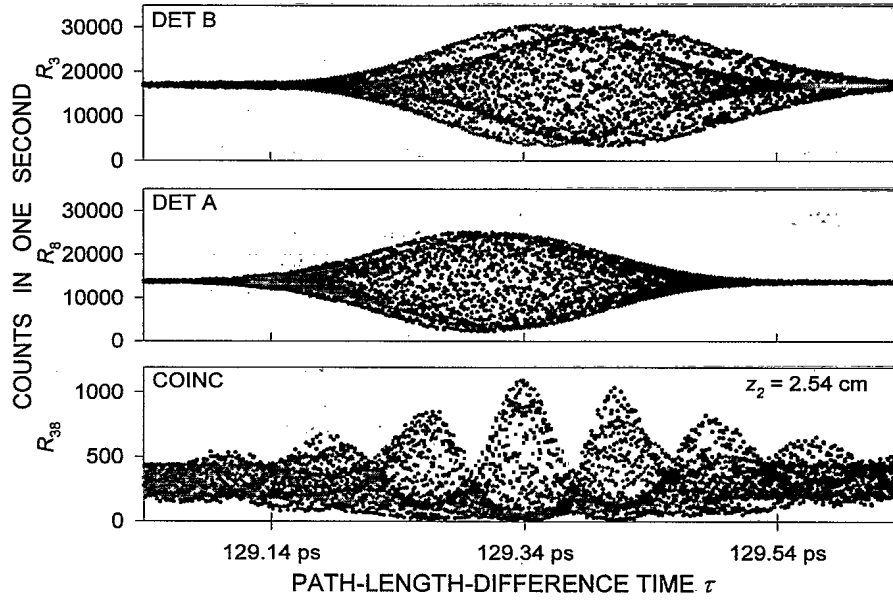
FIG. 8. Mach-Zehnder interference patterns for unbalanced dispersion with NSO. Experimental data (black dots) and theoretical results (gray dots) with $z_2 = 2.54$ cm of BK7 glass inserted in one arm of the interferometer ($z_1 = 0$). The upper panel shows the counts recorded by detector B, the middle panel shows the counts recorded by detector A, and the lower panel shows the counts recorded in coincidence between detectors A and B. The vertical scale represents the number of counts recorded in one second for each path-length-difference time τ (corresponding to a different position of the retroreflector).

$$R_4(\tau) = N_4 \left\{ \frac{1}{2} - \frac{V_4}{4}[f(\tau, \omega_1) - f(\tau, \omega_2)] \right\}, \quad (6')$$

$$R_{34}(\tau) = N_{34} \left[\frac{1}{2} + \frac{V_{34}}{4}[g(\tau) + h(\tau)] \right], \quad (8')$$

$$R_3(\tau) = N_3 \left[\frac{1}{2} - \frac{V_3}{2}f(\tau, \omega_2) \right], \quad (11')$$

$$R_8(\tau) = N_8 \left[\frac{1}{2} - \frac{V_8}{2}f(\tau, \omega_1) \right], \quad (12')$$

$$R_{38}(\tau) = N_{38} \left\{ \frac{1}{4} - \frac{V_{38}}{4}[f(\tau, \omega_1) + f(\tau, \omega_2)] \right.$$
$$\left. + \frac{V_{38}}{8}[g(\tau) + h(\tau)] \right\}. \quad (13')$$

The quantities $f(\tau)$, $g(\tau)$, and $h(\tau)$ are precisely those defined in Eqs. (7), (9), and (10) above. The visibilities of the sum-frequency terms, in the region of large τ, are $\frac{1}{2}V_{34}$ for FSO and $\frac{1}{2}V_{38}$ for NSO.

Satisfactory fits to the data in Fig. 7 for FSO, shown as gray dots, were obtained by using Eqs. (5'), (6'), and (8') with the values $V_3 = V_4 = V_{34} = 0.7$, $N_3 = 29\,684$, $N_4 = 29\,088$, and $N_{34} = 475.96$. Satisfactory fits to the data in Fig. 8 for NSO, also shown as gray dots, were obtained by using Eqs. (11'), (12'), and (13') with the values $V_3 = V_8 = 0.8$, $V_{38} = 0.85$, $N_3 = 33\,904$, $N_8 = 27\,628$, and $N_{38} = 1258.89$. In both cases we chose $\lambda_p = 413.1$ nm, $\lambda_1 = 840.0$ nm, $\lambda_2 = 812.8$ nm, and $\sigma = 1.25 \times 10^{13}$ s^{-1}. The values of β_0, β_1, and β_2 were provided in Sec. II C.

Though the fits of the data to the theory are reasonable, they are hardly perfect. The lack of agreement is not unexpected because of the idealized nature of the simple joint Gaussian state used for the calculations presented here. We have determined that the fits can be substantially improved by phenomenologically incorporating additional parameters

in the equations (though we do not demonstrate this here). Indeed, a more thorough treatment of the down-conversion process that accounts for finite pump-beam waist, pump spectral width, and crystal length yields a state that contains additional parameters [15,16]. The interference patterns obtained by using this more sophisticated description are substantially more complex than those presented here and are expected to provide a superior match with the experimental results [20].

C. Balanced dispersion

In Figs. 9 and 10 we present the results of balanced dispersion experiments, with $z_2 = 2.54$ cm and $z_1 = 2.54$ cm, for FSO and NSO, respectively. As discussed in Sec. II B, the patterns should be the same as those obtained in the nondispersive case and indeed they are. They are well represented by the results displayed in the upper-left quadrants of Figs. 4 and 5, respectively ($z_2 = z_1 = 0$). The gray dots, which represent the fits to the data in Fig. 9 for FSO, were obtained by using Eqs. (5'), (6'), and (8') with the values $z_2 = z_1 = 0$, $V_3 = V_4 = V_{34} = 0.7$, $N_3 = 26\,692$, $N_4 = 24\,998$, and $N_{34} = 417.27$. The gray dots in Fig. 10 for NSO were obtained by using Eqs. (11'), (12'), and (13') with the values $z_2 = z_1 = 0$, $V_3 = V_8 = 0.8$, $V_{38} = 0.85$, $N_3 = 32\,254$, $N_8 = 25\,408$, and $N_{38} = 1087.6$. In both cases we again set $\lambda_p = 413.1$ nm, $\lambda_1 = 840.0$ nm, $\lambda_2 = 812.8$ nm, and $\sigma = 1.25 \times 10^{13}$ s^{-1}.

IV. CONCLUSION

We have observed a variety of unusual fourth-order interference patterns when nondegenerate photon pairs are fed into single and dual Mach-Zehnder interferometers in which dispersive elements have been deliberately placed. The singles rates, reflecting second-order interference, are affected by dispersion in the usual manner expected for clas-
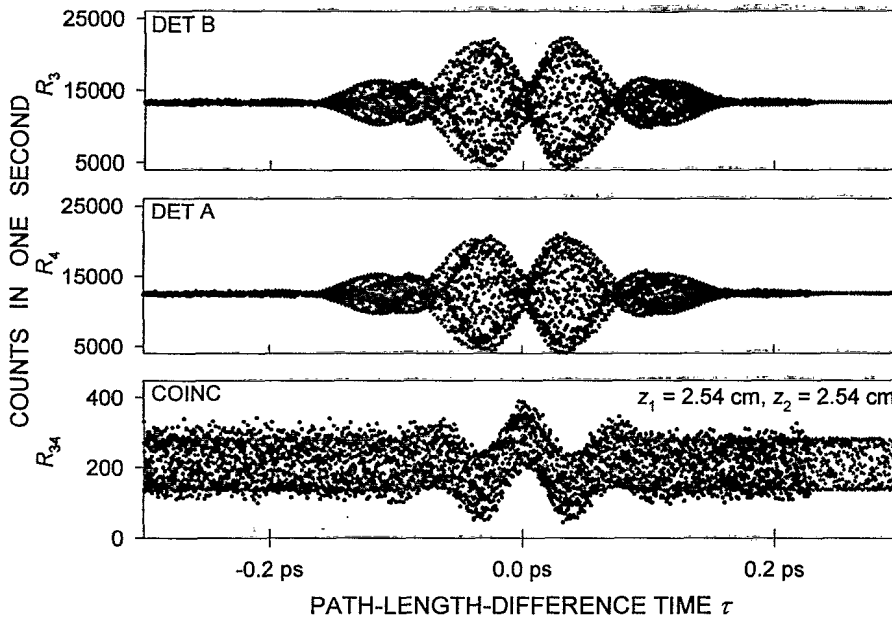
FIG. 9. Mach-Zehnder interference patterns for balanced dispersion with FSO. Experimental data (black dots) and theoretical results (gray dots) with 2.54 cm of BK7 glass inserted into each arm of the interferometer ($z_1 = z_2 = 2.54$ cm).

sical fields. However, the anticorrelation in the frequencies of the down-converted pair photons gives rise to nonlocal behavior that can, under certain conditions, allow the cancellation of dispersive broadening in the coincidence rate, reflecting fourth-order interference. Complete cancellation occurs for dispersive materials that obey $\beta_1(\omega_1) = \beta_1(\omega_2)$ and $\beta_2(\omega_1) = -\beta_2(\omega_2)$. In this case, the second- and fourth-order interference patterns are the same as those obtained in the nondispersive case. Although they decay, the difference frequency oscillations are highly robust.

Many fourth-order interference experiments carried out previously, using both degenerate and nondegenerate photon pairs, have revealed the existence of nonlocal pump-frequency oscillations in the coincidence rate that continue for large path-length-difference times. We have shown, both theoretically and experimentally, that these oscillations persist in the presence of dispersion, although in general their visibility is reduced. However, for unbalanced dispersion using materials that possess the special characteristics $\beta_1(\omega_1) = \beta_1(\omega_2)$ and $\beta_2(\omega_1) = -\beta_2(\omega_2)$, and for balanced dispersion, the pump-frequency oscillations have precisely the same visibility as they do in the absence of dispersion, as is evident from Eq. (9).
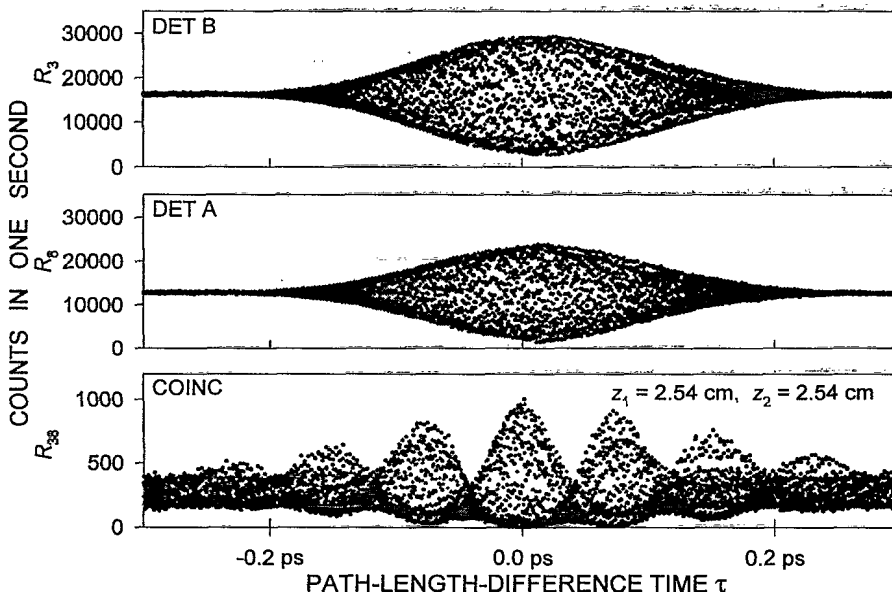
ACKNOWLEDGMENTS

FIG. 10. Mach-Zehnder interference patterns for balanced dispersion with NSO. Experimental data (black dots) and theoretical results (gray dots) with 2.54 cm of BK7 glass inserted into each arm of the interferometer ($z_1 = z_2 = 2.54$ cm).

[1] L. Mandel, Ann. N.Y. Acad. Sci. **755**, 1 (1995).

[2] Z. Y. Ou and L. Mandel, Quantum Opt. **2**, 71 (1990).

[3] J. Peřina, Z. Hradil, and B. Jurčo, *Quantum Optics and Fundamentals of Physics* (Kluwer, Boston, 1994).

[4] J. D. Franson, Phys. Rev. A **45**, 3126 (1992).

[5] D. C. Burnham and D. L. Weinberg, Phys. Rev. Lett. **25**, 84 (1970).

[6] S. Friberg, C. K. Hong, and L. Mandel, Phys. Rev. Lett. **54**, 2011 (1985).

[7] A. M. Steinberg, P. G. Kwiat, and R. Y. Chiao, Phys. Rev. A **45**, 6659 (1992); Phys. Rev. Lett. **68**, 2421 (1992).

[8] C. K. Hong, Z. Y. Ou, and L. Mandel, Phys. Rev. Lett. **59**, 2044 (1987).

[9] J. G. Rarity, Ann. N.Y. Acad. Sci. **755**, 624 (1995).

[10] J. H. Shapiro and K.-X. Sun, J. Opt. Soc. Am. B **11**, 1130 (1994).

[11] R. A. Campos, B. E. A. Saleh, and M. C. Teich, Phys. Rev. A **42**, 4127 (1990).

[12] G. S. Agarwal and S. D. Gupta, Phys. Rev. A **49**, 3954 (1994).

[13] T. S. Larchuk, R. A. Campos, J. G. Rarity, P. R. Tapster, E. Jakeman, B. E. A. Saleh, and M. C. Teich, Phys. Rev. Lett. **70**, 1603 (1993).

[14] J. G. Rarity, P. R. Tapster, E. Jakeman, T. S. Larchuk, R. A. Campos, M. C. Teich, and B. E. A. Saleh, Phys. Rev. Lett. **65**, 1348 (1990).

[15] A. Joobeur, B. E. A. Saleh, and M. C. Teich, Phys. Rev. A **50**, 3349 (1994).

[16] A. Joobeur, B. E. A. Saleh, T. S. Larchuk, and M. C. Teich (unpublished).

[17] B. E. A. Saleh and M. C. Teich, *Fundamentals of Photonics* (Wiley, New York, 1991).

[18] Schott Optical Glass Catalog (Schott Glass Technologies, Inc., Duryea, PA 18642), 1992.

[19] T. S. Larchuk, M. C. Teich, and B. E. A. Saleh, Ann. N.Y. Acad. Sci. **755**, 680 (1995).

[20] A. Joobeur, B. E. A. Saleh, and M. C. Teich (unpublished).